

Contents lists available at ScienceDirect

Acta Materialia

journal homepage: www.elsevier.com/locate/actamat



Full length article

Microstructure based fatigue life prediction framework for polycrystalline nickel-base superalloys with emphasis on the role played by twin boundaries in crack initiation



Saikumar R. Yeratapally ^a, Michael G. Glavicic ^b, Mark Hardy ^c, Michael D. Sangid ^{a,*}

- ^a School of Aeronautics and Astronautics, Purdue University, West Lafayette, IN 47907, USA
- ^b Rolls-Royce Corporation, Indianapolis, IN 46225, USA
- c Rolls-Royce plc, Derby, DE24 8BJ, UK

ARTICLE INFO

Article history: Received 17 July 2015 Received in revised form 13 January 2016 Accepted 18 January 2016 Available online xxx

Keywords:
Fatigue crack initiation
Twin boundaries
Persistent slip bands
Elastic anisotropy
Plastic strain accumulation

ABSTRACT

Fatigue crack initiation in polycrystalline materials is dependent on the local microstructure and the deformation mechanism, and can be attributed to various mechanistic and microstructural features acting in concert like the elastic stress anisotropy, plastic strain accumulation, slip-system length, and grain boundary character. In nickel-base superalloys, fatigue cracks tend to initiate near twin boundaries. The factors causing fatigue crack initiation depend on the material's microstructure, the variability of which results in the scatter observed in the fatigue life. In this work, a robust microstructure based fatigue framework is developed, which takes into account i) the statistical variability of the material's microstructure, ii) the continuum scale complex heterogeneous 3D stress and strain states within the microstructure, and iii) the atomistic mechanisms such as slip-grain boundary (GB) interactions, extrusion formations, and shearing of the matrix and precipitates due to slip. The quantitative information from crystal plasticity simulations and molecular dynamics is applied to define the energy of persistent slip bands (PSB). The energy of a critical PSB and its associated stability with respect to the dislocation motion is used as the failure criterion for crack initiation. This unified framework provides us with insights on why twin boundaries act as preferred sites for crack initiation. In addition to that, the computational framework links scatter observed in fatigue life to variability in material's microstructure. © 2016 Acta Materialia Inc. Published by Elsevier Ltd. All rights reserved.

1. Introduction

Fatigue scatter observed in components made of polycrystalline materials can be partly attributed to the variability of complex heterogeneities in the microstructure. These heterogeneities are responsible for the complex stress and strain fields developed under load, and govern where cracks could potentially nucleate. Empirical life prediction methods [1,2] cannot relate fatigue life to the variability in microstructure. Although there has been substantial work done in using advanced computational tools and experimental techniques to understand the driving forces for fatigue crack initiation, there is still a considerable amount of work to do in calculating fatigue scatter by explicitly taking into consideration the heterogeneities of a given material's microstructure and

the complicated 3D stress and strain states that develop within the bulk of the material. The current work discusses a computational fatigue framework which fills this gap by linking virtual microstructures that resemble real material's microstructure in a statistical sense, to a fatigue life prediction model. This life prediction model within the fatigue framework defines crack initiation based on the stability of persistent slip bands (PSBs) as they interact with grain boundaries (GBs).

During fatigue loading, dislocations multiply and accumulate within the material resulting in an increased value of the dislocation density. These dislocations arrange themselves in the lowest energy configurations by forming clusters of dipoles [3–5]. As a consequence, strain is localized into thin slip bands called PSBs, which are precursors for crack initiation. In polycrystalline metals, PSBs consist of alternating high and low dislocation density zones, representing a ladder-like structure [6,7]. In precipitation hardened materials, like nickel-base superalloys, PSBs form as dislocations cut through the γ matrix and γ' precipitates in a planar slip manner

Corresponding author.

E-mail address: msangid@purdue.edu (M.D. Sangid).

[8,9]. Essman, Mughrabi, and co-workers have done extensive work in understanding strain localization in PSBs and establishing the formation of extrusions, intrusions, and microcracks due to interaction of PSBs with surfaces and GBs [6,7,10]. PSBs were observed to pass through low angle grain boundaries (LAGB) unhindered, where as they are impeded by high angle grain boundaries (HAGB). The PSB-HAGB interaction results in the formation of dislocation pile-ups, which increase stress concentrations at the PSB-GB interface, ultimately leading to the formation of microcracks [11]. The topic of PSB formation in polycrystalline metals and alloys has been discussed extensively in literature surveys [12-14]. The experimental observations pertaining to the structure of the PSB and its interaction with GBs are taken into consideration while formulating the energy of a PSB, whose stability will be used to define crack initiation in the fatigue framework discussed in the current study.

Microcracks were observed to nucleate at the twin boundaries (TBs) in certain FCC polycrystalline metals [11,15–17] and alloys [18–22]. Over the past three decades, studies have searched for an understanding of why TBs are preferred sites for fatigue crack initiation. Wang et al. used a finite element model on a bi-crystal with a TB and found that stress and slip enhancement is greatest in a small volume of material near the surface and close to the TB [23]. Peralta et al. calculated the compatibility stresses at TBs and varied the orientation of the loading axis to the TB [24]. They observed that the stress concentration at the TB is a maximum when the tensile axis is applied along a <111> direction. Neumann derived an analytical expression for the tractions at the intersection of a TB and a surface, and further emphasized that the observed slip activity and the crack initiation on planes parallel to the TB plane is not due to the compatibility stresses, but due to the logarithmic singular surface tractions that occur at the intersection of the surface with the TB [25]. In addition to simple bicrystal based models, which teach us about activity in the local neighborhood of a TB, high fidelity models that take into account heterogeneous deformation of twins and energetics of twin-slip interactions have also been developed.

Sangid et al. using molecular dynamics (MD) simulations, showed that coherent TB offers the lowest interface energy and highest barrier to dislocation nucleation and transmission, thus providing a significant strengthening contribution [26]. Further, Sangid et al. developed a microstructure-based model to predict fatigue crack nucleation in a nickel-base superalloy, U720, consisting of a high density of coherent TBs [22,27,28]. Their model, which takes into account the energetics of GBs and the interaction of PSBs with GBs, predicted that most often cracks nucleated at TBs in U720, which was also observed in experiments [22]. By calculating a fatigue indicator parameter in a crystal plasticity framework, Castelluccio and McDowell showed that large annealing twins are more detrimental than thinner deformation twins and stressed their importance [29]. Further, Cerrone et al. used gradient crystal plasticity in a finite element model of an experimentally measured 3D microstructure wherein a microcrack nucleated along a coherent TB in a nickel-base superalloy, LSHR [30]. From the crystal plasticity simulations, they hypothesized that high elastic anisotropy and coplanarity of the boundary plane with a {111} slip plane were responsible for the accumulation of slip and subsequently for the microcrack nucleation event at the TB. Each of the aforementioned analytical and computational models provide valuable insights into the role played by TBs on fatigue crack initiation in polycrystalline materials. But understanding why fatigue cracks initiate at twins from a lengthscale point of view is still lacking. The fatigue framework presented in the current study takes into account, the energetics of slip-twin interaction (calculated using MD), and the quantitative information from the complicated stress/strain states developed within the twin (obtained from crystal plasticity simulations) and uses this information in a failure prediction model. A focus of the current study (which explicitly considers TBs in the microstructure) is to understand the effect of elastic anisotropy, plastic strain accumulation and normal stress on crack initiation at twins.

Fatigue crack nucleation is a microstructure and deformation mechanism based phenomenon and a robust fatigue prediction model should consider contributions from various length scales. Although there has been substantial and important work done using crystal plasticity based models and MD simulations, the present work develops a framework, which unifies length scales (by considering both atomistic and continuum level contributions) with explicit consideration of microstructures. Such a high fidelity model helps us gain more insight into the most critical factors that contribute to crack nucleation and also link microstructure variability to scatter observed in fatigue life. This framework takes quantitative information of the heterogeneous deformation from crystal plasticity simulations pertaining to microstructure descriptions of 3D stresses and strains, energetics of slip-GB interaction, stacking fault and anti-phase boundary energies from atomistic calculations, to predict where cracks could potentially nucleate. Further, this framework explicitly includes twins in statistically equivalent microstructures (SEMs) that are built on the morphological and crystallographic statistics obtained from the real material's microstructure data. The present work also delivers insights on the evolution of elastic anisotropy and plastic strain accumulation at the GBs. The development of SEMs based on the microstructure of the material of interest is discussed in Section 2. Section 3 discusses the formulation of the PSB energy based, microstructure dependent fatigue framework. The integration of the results from crystal plasticity based simulations and the fatigue model of PSBs are discussed in this section. Section 4 includes results and discussion. Conclusions are presented in Section 5.

2. Material characterization and statistically equivalent microstructure (SEM)

A nickel-base superalloy, RR1000, developed by Rolls-Royce plc is used in this study. The material produced using powder metallurgy process underwent forging and was heat-treated above the γ' solvus (at 1170 °C) for 5 h [21]. RR1000 is a precipitation hardened material and the ordered γ' precipitates present in the material provide a strengthening mechanism and stability at elevated temperatures. The heterogeneities present in the microstructure are quantified based on experimental electron backscatter diffraction (EBSD) data. These complex heterogeneities govern strain localization within the material and affect fatigue life. Quantitative characterization of the microstructure provides information on grain size distribution, orientation distribution (to understand texture of the material), misorientation distribution (to spatially understand the neighbor orientations) and grain boundary character distribution of special type of GBs called coincident site lattice (CSL) GBs. Such a characterization not only helps in linking microstructure to properties but also provides benchmark statistics based on which statistically equivalent microstructures (SEMs) can be generated. SEMs are virtual microstructures, built to statistically represent the (morphological and crystallographic) heterogeneities of the microstructure of the material, as closely as possible, as well as the strength properties of the material (but not necessarily the extreme values for fatigue as discussed in Section 4).

In order to enhance the predictive capabilities of the microstructure based failure prediction model, the representation of the microstructure must capture the variability observed in the material. For this purpose, the statistics of the different morphological and crystallographic characteristics mentioned above are accounted for, while creating the SEMs that are representative of RR1000. Texture of RR1000 was observed to be random. Hence, a random texture definition was assigned to the SEMs generated.

The data at hand is the 2D microstructure of the material that is derived from an EBSD scan of the material. To fully characterize grain structure, direct 3D data is a necessity, but due to the lack of availability of the 3D material data, certain (stereological and other modeling) assumptions have to be made while transitioning from 2D to 3D. Two main assumptions are made in obtaining the 3D grain size distribution from the 2D grain size distribution. First, it is assumed that the grain size in the 3D SEM would follow a lognormal distribution. This appears to be a valid assumption as a wide variety of metals and alloys have a lognormal grain size distribution [31]. The second assumption is to scale the 2D grain sizes obtained from EBSD data, with a stereological scaling factor $\frac{4}{11}$. Groeber [32] showed that this scaling is reasonable and the error is within 5% by comparing the scaled data obtained from 2D microstructure data of a nickel-base superalloy, IN100, with 3D microstructure data

Grain shape distributions are not as straight forward as the grain size distributions. The irregular geometries that are typical features of grains in a polycrystalline material make it difficult to unambiguously describe the shapes of grains. Due to the lack of availability of the 3D data of RR1000, the grain shape distribution parameter (in the form of moment invariants) information was extracted from the experimental 3D data set of a sub-solvus heat treated nickel-base superalloy, IN100 [33]. This information was input into DREAM.3D [33,34] to define the shapes of the grains in the equivalent microstructure.

A characteristic feature of the microstructure of RR1000 is the considerably high number of annealing twins. Hence the grain boundary character distribution of the SEMs generated should show a high frequency of annealing twins to mimic the real microstructure as closely as possible. Annealing twins were inserted into the microstructure using a twin-insertion code [35]. The twin-insertion code chooses one of the four variants (and their conjugates) of the <111> planes at random and the corresponding grain orientation for the twin is calculated by rotating the orientation of the parent grain 60° about the same <111> variant that was chosen. The percentage of annealing TBs (with respect to all CSL GBs in the SEM) in the SEMs closely matched the values observed in real microstructure data. All the twins inserted into the microstructure are continuous within their respective parent grain and do not have discontinuities like steps or ledges.

The statistics obtained from the 2D characterization of the material followed by stereological assumptions is input into the StatGenerator toolbox in DREAM.3D, which creates SEMs, following which surface meshes of these microstructures can be generated. These surface meshes were converted into a volume mesh using parallelized polycrystal mesher (PPM) [36]. Fig. 1 gives a brief overview of the process involved in the generation of SEMs, which are then volume meshed to be used in a crystal plasticity finite element framework.

3. PSB energy based fatigue model

Over the past three decades, various micro-mechanical fatigue crack initiation models have been developed that consider the energy of dislocation structure within PSBs [22,27,28,37]. Tanaka and Mura define crack initiation at a point when the total energy of the PSB equals the specific fracture energy of the material [37]. Sangid et al. formulated the energy of a PSB within a polycrystalline nickel-base superalloy using energy contributions from atomistic and continuum length scales, and defined crack initiation to occur

at a point when the PSB reaches a minimum energy configuration [22,27,28]. The aforementioned models do not account for a complex 3D stress state evolving within each grain of the polycrystal, e.g. the previous models use Schmid factors to calculate resolved shear stress on a slip system. The model presented in the current study uses a modified version of the energy expression developed by Sangid et al. [22,27,28], by taking the outputs of crystal plasticity finite element (CPFE) based calculations, including the normal stress, resolved shear stress and accumulated strain in a slip system. This information along with the GB energetics is fed into PSB model (discussed below) to predict the potential location of crack nucleation.

Fig. 2 displays a schematic of a PSB formed in a nickel-base superalloy, based on shearing of γ' precipitates. In the schematic shown, a PSB traverses a LAGB and is impeded by a HAGB (for example an annealing TB), where the dislocations pile-up, form extrusions at the boundary plane, and thereby concentrates stress at the boundary. With this established view of a PSB (based on experimental observations), we define the energy of a PSB as follows:

$$E_{PSB} = \ E_{atomistic \ scale \ contributions} + \ E_{continuum \ scale \ contributions} \ \ (1)$$

$$\begin{split} E_{atomistic \ scale \ contributions} &= E_{\gamma \ and \ \gamma^{'} shearing} \\ &+ E_{extrusion \ formation \ at \ GBs} \end{split} \tag{2}$$

$$\begin{split} E_{\gamma \text{ and } \gamma' \text{ shearing}} &= \sum_{i} \partial X_{i} \left(f \int_{0}^{L} \gamma_{\text{APB}} dL \right. \\ &+ \left. (1 - f) \int_{0}^{L} \gamma_{\text{SFE}} dL \right) n_{\text{eff}}^{\text{layers}} \end{split} \tag{3}$$

$$E_{extrusion \; formation \; at \; GBs} = \; \sum_{i} \partial X_{i} \Big(E_{slip-GB}^{\gamma-MD} n_{ext-GB}^{dis} bh \Big) \eqno(4)$$

$$\begin{split} E_{continuum \ scale \ contributions} = & -E_{applied \ work} - E_{hardening} \\ & + E_{nile-up} \end{split} \tag{5}$$

$$E_{applied\ work} = \sum_{i} \partial X_{i} \Big(b L n^{layers} \Delta \tau_{CPFEM}^{\alpha} \Big) \eqno(6)$$

$$E_{hardening} = \sum_{i} \partial X_{i} \Big(b L n^{layers} \sigma_{hardening} \Big)$$
 (7)

$$E_{pile-up} = \sum_{i} \partial X_{i} \Big(b L n^{layers} \sigma_{pile-up} \Big) \tag{8} \label{eq:epile-up}$$

Putting all the above energy expressions together, the total energy of a PSB is mathematically expressed as follows:

$$\begin{split} E_{PSB} &= \sum_{i} \partial X_{i} \left(f \int_{0}^{L} \gamma_{APB} dL + \ (1-f) \int_{0}^{L} \gamma_{SFE} dL \right) n_{eff}^{layers} \\ &+ \sum_{i} \partial X_{i} \Big(E_{slip-GB}^{\gamma-MD} n_{ext-GB}^{dis} bh \Big) + \sum_{i} \partial X_{i} \Big(\sigma_{pile-up} \\ &- \Delta \tau_{CPFEM}^{\alpha} - \sigma_{hardening} \Big) bL n^{layers}, \end{split} \tag{9}$$

where ∂X_i is the incremental slip within PSB, f is the volume

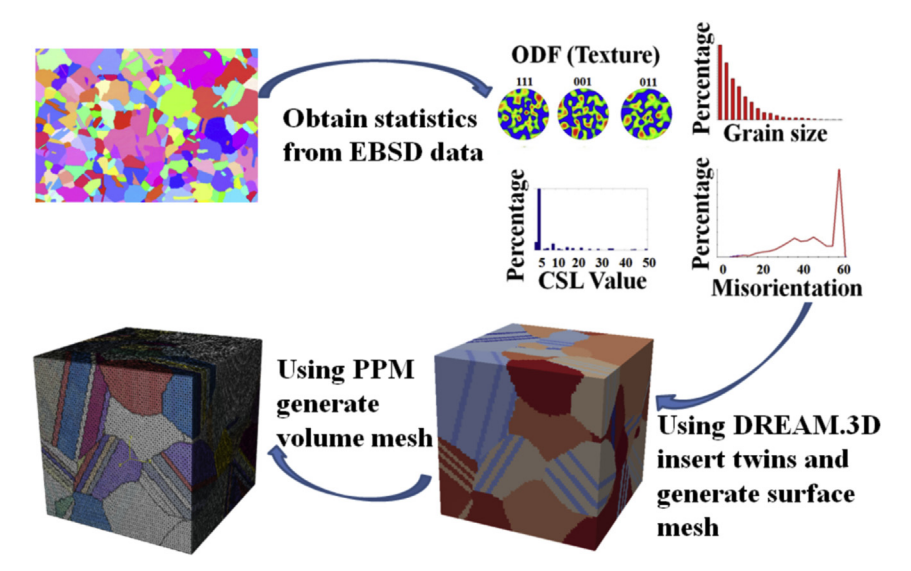


Fig. 1. Workflow for generating statistically equivalent microstructures.

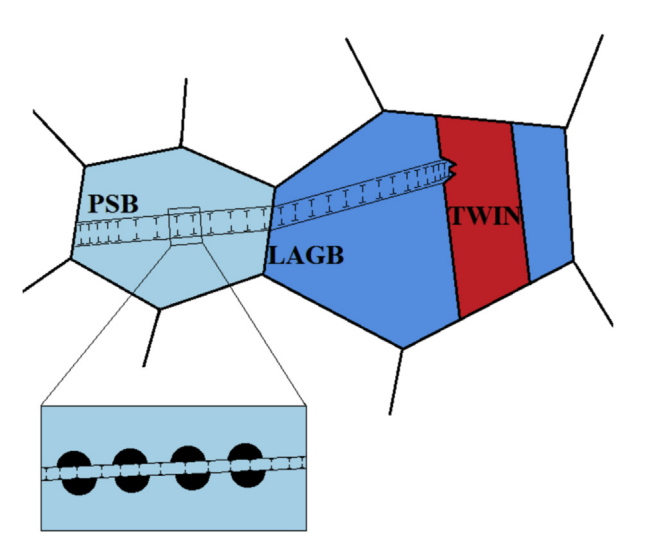


Fig. 2. Schematic of a PSB.

fraction of the γ' precipitate phase, γ_{SFE} is the stacking fault energy of the γ phase, γ_{APBE} is the anti-phase boundary energy of the γ' precipitate, n_{eff}^{layers} is the number of effective layers contributing to SFE or APBE, L is the length of the PSB, $E_{slip_GB}^{\gamma-MD}$ is the energy required for a dislocation to transmit across a GB, $n_{ext_GB}^{dis}$ represents the number of dislocations forming an extrusion at the GB, b is the magnitude of the Burgers vector, h is the width of the PSB, $\Delta\tau_{CPFEM}^{\alpha}$ is applied cyclic stress on the PSB, $\sigma_{hardening}$ accounts for the hardening within the PSB, σ_{pile_up} is the pile-up stress at the intersection of the PSB and the GB, and n^{layers} is the number of slip planes within the PSB, which is related to the PSB width, h as $n^{layers} = \frac{h}{h}$.

Failure (e.g. fatigue crack initiation) would occur when the energy of the PSB would attain its minimum value. Mathematically speaking, cracks would initiate when the following condition is satisfied:

$$\frac{\partial E_{PSB}}{\partial X_i} = 0. \tag{10}$$

3.1. Atomistic level contributions

Atomistic level deformation mechanisms which contribute to fatigue failure are taken into consideration in the current fatigue model. Dislocations exist within a PSB by shearing the matrix and the γ' precipitates and pile-up at the GBs to form extrusions. The energy that goes into aforementioned deformation mechanisms was calculated using MD simulations in LAMMPS [38].

3.1.1. Shearing of matrix and precipitates

At intermediate temperatures, dislocations were observed to shear γ' precipitates in RR1000 [39]. For a dislocation within a PSB to shear through the γ matrix (Ni) and γ' precipitate (Ni_3Al), it has to overcome the energies associated with destroying the stacking sequence of an FCC structured Ni and an ordered L1_2 structured Ni_3Al, which are defined as the stacking fault energy (SFE) and the anti-phase boundary energy (APBE), respectively. Embedded atom potentials from Foiles—Hoyt [40] and Mishin [41] were used to calculate the SFE and APBE curves for γ and γ' phases, respectively. Based on these energies, the total energy required by a PSB of length L, to shear through a matrix and precipitate phase is given by:

$$E_{\gamma \text{ and } \gamma' \text{ shearing}} = \sum_{i} \partial X_{i} \left(f \int_{0}^{L} \gamma_{\text{APB}} dL + (1 - f) \int_{0}^{L} \gamma_{\text{SFE}} dL \right) n_{\text{eff}}^{\text{layers}}. \tag{11}$$

In multi-axial fatigue, the critical plane is a combination of having the maximum normal stress and shear strain according to the description of Fatemi—Socie [42]. The concept of normal stress acting as a driving force for crack initiation [42] and growth has been extended to microstructural sensitive fatigue models [29], which is adopted in this analysis. It is established that SFE and APBE are affected by an application of normal strain on the slip system [43,44]. As depicted in Fig. 3, the application of tensile normal load moves the atom layers apart which makes it easy for slip to occur on the slip planes, thereby reducing the SFE (or APBE) and vice

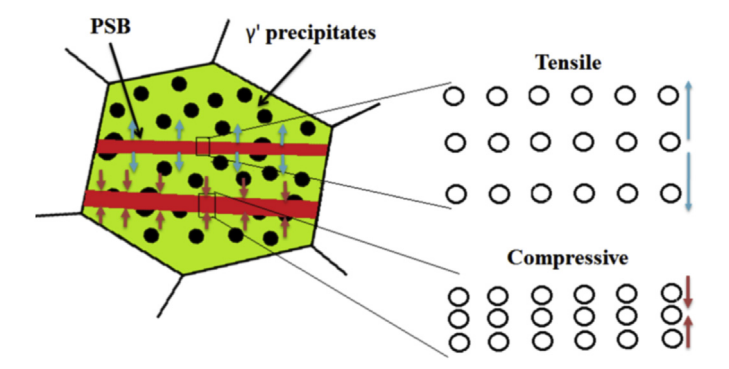


Fig. 3. Schematic of normal strain acting on PSB, stretching (or compressing) the lattice, shown in the inlet figures.

versa. SFE and APBE curves (for Ni and Ni₃Al phases respectively) have been plotted for various normal strains (Fig. 4a and b). The normal strains were applied along the <111> direction perpendicular to the slip planes. It is evident from the plots that the respective energies increased with an application of compressive normal strain and decreased with an application of tensile normal strain consistent with previous studies [43,44].

3.1.2. Extrusion formation

As discussed earlier, a PSB is impeded by a HAGB, and due to this, the dislocations within the PSB pile-up at the GB. Stress concentration at the GB increases and leads to activation of slip systems in the neighboring grains. As a result, dislocations could be partially transmitted across the GB leaving behind a residual dislocation at the GB [46]. The discontinuous nature of slip and strain incompatibility at GBs leads to slip irreversibilities and hence extrusion formation, with repeated cyclic loading [13]. This in turn raises the stress concentrations at the PSB-GB interface due to extrusion formation. The energy needed for a dislocation to form an extrusion depends on the type of the GB, thus the fatigue model incorporates local affects of each specific type of GB's resistance to slip transmission. From the plot in Fig. 5 (reproduced from Sangid et al. [27]), TB offers the highest barrier to dislocation transmission.

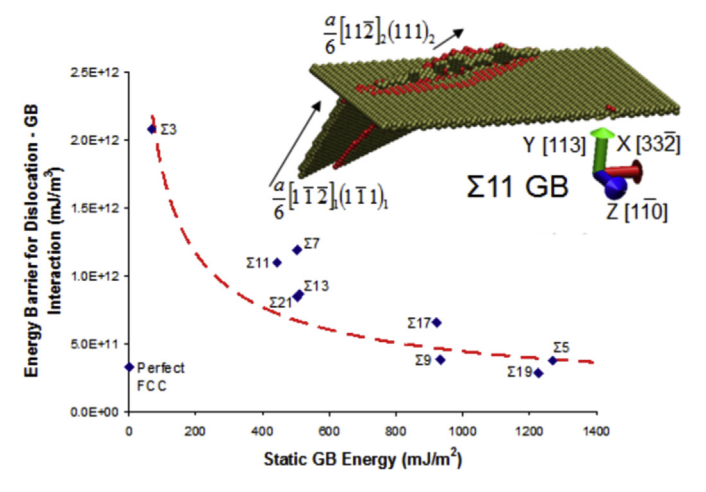


Fig. 5. Energy barrier for dislocation transmission across various types of CSL GBs (figure taken from Sangid et al. [27]).

Depending upon the type of the GB and the number of dislocations forming an extrusion at the GB, the energy required by a PSB to form an extrusion, E_{extrusion formation at GBs}, is given as follows:

$$E_{extrusion \; formation \; at \; GBs} = \; \sum_{i} \partial X_{i} \Big(E^{\gamma-MD}_{slip-GB} n^{dis}_{ext-GB} bh \Big). \eqno(12)$$

The calculation of number of dislocations penetrating a GB, $n_{\rm ext-GB}^{\rm dis}$, is not straight forward and it was calculated based on empirical relations. In order to consider the evolution of cyclic slip irreversibilities due to formation of extrusions, empirical formulation of extrusion growth with an increasing number of cycles is incorporated into the model, as rigorous experimental data are not available for the evolution of extrusion at GBs. There is a vast amount of work done in understanding how PSBs evolve at the surface. Risbet et al. [9,47] measured extrusion heights at the surface of a nickel-base superalloy using AFM techniques. It was observed that extrusions appeared after a threshold number of loading cycles, $n_{\rm offset}$. The number of dislocations within the

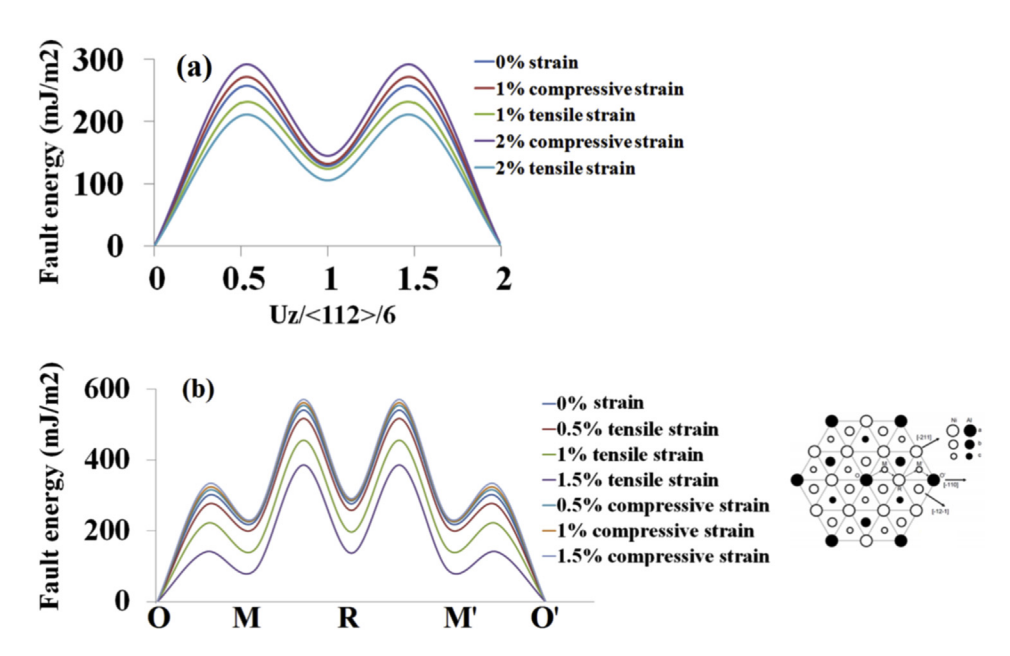


Fig. 4. (a) SFE curve for various applied normal strains. (b) APBE curve for various applied normal strains, (inlet schematic was redrawn based on schematic from Rice et al. [45]).

extrusions is assumed to follow a square root dependency on the number of fatigue cycles, based on the model of Essmann, Gösele, Mughrabi [6]:

$$n_{\text{ext-GB}}^{\text{dis}} \alpha \sqrt{n - n_{\text{offset}}},$$
 (13)

where n_{offset} is calculated based on the condition that the applied stress $(\tau^{\alpha} + \ \sigma_{pile-up})$ on a dislocation within a PSB impinging upon the GB must be greater than the transmission resistance offered by the GB. This GB resistance to PSBs is calculated using Stroh's formulation [48] assuming that the PSB is favorably aligned to the GB to form extrusions and hence initiate a crack. Christ [49] used this relation of GB cracking due to pile-ups to study PSB-GB interaction. Their expression calculates the stress required by a pile-up to nucleate a crack, which was formulated to be dependent on the surface energy (γ) of the material. We replace this term with the GB energy calculated from MD simulations to quantify various GBs resistance to dislocation transmission and extrusion formation. Hence the model calculates n_{offset} based on the condition that extrusions would cross a GB when the applied stress $(\tau^{\alpha} + \ \sigma_{pile-up})$ is greater than the GB resistance (σ_{stroh} , see Eq. (16)). Also the number of dislocations that penetrate the GB increases with an increase in the applied stress:

$$n_{ext-GB}^{dis} \ \alpha \ \frac{\tau^{\alpha} + \sigma_{pile-up} - \sigma_{stroh}}{\sigma_{stroh}}, \eqno(14)$$

where the resolved shear stress τ^{α} is taken from CPFE calculations, $\sigma_{pile-up}$ is calculated based on the relation between long range pileup stresses in terms of slip system strain, formulated by Schouwenaars et al. [50] as follows:

$$\sigma_{pile-up} = \frac{1.8\mu\gamma^{\alpha}}{\pi(1-\nu)}.$$
 (15)

Here μ is rigidity modulus, ν is the poisson's ratio and γ^{α} is accumulated strain in the slip-system which is calculated from the CPFE simulations. As mentioned earlier, σ_{stroh} is calculated based on the Stroh's formulation [48], expressed as follows:

$$\sigma_{\text{stroh}} = \left\{ \frac{\pi E_{\text{GB}}^{\text{trans}} \mu}{2(1 - \nu)L} \right\}^{\frac{1}{2}}, \tag{16}$$

where E_{GB}^{trans} is the dislocation transmission energy [26] of a GB and its value for various types of CSL GBs is shown in Fig. 5, L is the length of the PSB. It is noted that n_{ext-GB}^{dis} depends on the pile-up length itself; more dislocations form extrusions from PSBs with large pile-up lengths and hence a length dependence is added to the model

$$n_{ext-GB}^{dis} \ \alpha \ \frac{L}{L_{avg}}, \eqno(17)$$

where L is the pile-up length and L_{avg} is the average pile-up length of all the PSBs formed.

Finally, a strain rate dependence is also established as to differentiate between slip systems with higher strain rate (which accumulate more slip and hence dislocations) and lower strain rates.

$$n_{ext-GB}^{dis} \ \alpha \ \frac{\dot{\gamma}^{\alpha}}{\dot{\gamma}_{0}}, \tag{18} \label{eq:18}$$

where $\dot{\gamma}^{\alpha}$ is the slip system strain rate and $\dot{\gamma}_{0}$ is the reference strain rate for all slip systems. It is added in the denominator for the

expression to be dimensionally consistent. From the flow rule used in the crystal plasticity formulation used in this framework (described in Section 3.3), we have $\dot{\gamma}^{\alpha} = \dot{\gamma}_{0} \left| \frac{\tau^{\alpha} - \chi^{\alpha}}{g^{\alpha}} \right|$, where m is the rate sensitivity parameter, τ^{α} is resolved slip-system stress, χ^{α} is back stress on a slip system and g^{α} is the critical resolved shear stress (CRSS). Combining the individual empirical formulations we define the number of dislocations penetrating the GB to form an extrusion, $n_{\text{ext}-GB}^{\text{dis}}$, as follows (by assuming proportionality constants in Eqs. (17) and (18) to be 1 for simplicity):

$$n_{ext-GB}^{dis} = \left| \frac{\tau^{\alpha} - \chi^{\alpha}}{g^{\alpha}} \right|^{m} \frac{L}{L_{avg}} \left(\frac{\tau^{\alpha} + \sigma_{pile-up} - \sigma_{stroh}}{\sigma_{stroh}} \right) \sqrt{n - n_{offset}}. \tag{19}$$

The PSB model uses energy barriers calculated from atomistic simulations for specific types of GBs. These values for the static GB energies (for distinct CSL GBs in Ni [27,51]), dislocation transmission energy barriers and dislocation nucleation energies for CSL GBs [27], stacking fault energy and anti-phase boundary energy values (shown in Fig. 4) are stored within a database and called within the PSB energy balance when needed (as the PSB encounters specific types of GBs within the microstructure). Using the energy values from a database makes the PSB model computationally very efficient, as MD simulations do not have to be run on a repetitive or hierarchical basis. These material models (relying on values, a priori, calculated and stored in databases) are easier to implement in practice due to their computational efficiency, as demonstrated by a spreadsheet based model developed by Parthasarathy et al. [52] to calculate the yield strength of superalloys.

3.2. Continuum level contributions

In the continuum scale, the PSB is subjected to an i) external stress field created due to the applied load, constrained deformation of neighboring grains and ii) internal stress fields due to long range pile-up stresses and hardening that occurs within the PSB. The continuum level description of dislocations contribution to the energy of a PSB is as follows:

$$\begin{split} E_{continuum \ scale \ contributions} &= \sum_{i} \vartheta X_{i} \Big(\sigma_{pile-up} - \Delta \tau_{CPFEM}^{\alpha} \\ &- \sigma_{hardening} \Big) b L n^{layers}. \end{split} \tag{20}$$

3.2.1. Applied stress

PSBs have been observed to form along one of the slip systems. Hence due to an applied load, these PSBs will be subjected to a resolved shear stress (RSS) acting on the slip system. In order to consider the role of the grain interaction and the complex 3D stress states that form within each grain, the RSS is directly taken from the CPFEM simulations. Within the CPFEM constitutive models [53], the RSSs are calculated by the expression $F^{eT}F^eS^*:(s^\alpha\otimes m^\alpha)$, where F^e is the elastic part of the deformation gradient (F = F^eF^p [54]), S^* is the 2nd Piola Kirchoff stress, $(s^\alpha\otimes m^\alpha)$ is the Schmid tensor. It is assumed in this model that PSB forms on the slip system with maximum RSS. Hence $\Delta\tau_{CPFEM}^\alpha$ is calculated based on the slip system which showed a maximum range of resolved shear stress over a cycle.

It is also observed that for the most active slip system within a grain (composed of thousands of material points in the finite element mesh) the percentage of standard deviation of RSS with respect to the average value of RSS calculated over all material points is less than 5% showing that if it is an active slip system then

all the material points have similar values of resolved shear stress with an error of $\pm 5\%$. On the contrary, if the slip system is inactive (with the RSS less than the CRSS) then the percentage of standard deviation of RSS with respect to the average value of RSS calculated over all material points is greater than 40%, inferring the large variance of RSS values over the domain of the material points that belong to that particular grain. Following this argument based on statistical observation, we compute the average resolved shear stress of all the slip systems, and only consider the maximum value (pertaining to the most active slip system) from the twelve obtained values. The maximum RSS value is used in the energy expression of the PSB. Therefore, the applied cyclic stress $\Delta \tau_{CPFEM}^{\alpha}$ is calculated for the most active slip system, in an average sense over all material points that belong to a grain. The $\Delta\tau_{CPFEM}^{\alpha}$ is calculated from peak to minimum applied load, thus accounting for the cyclic nature of fatigue.

3.2.2. Dislocation pile-up

As discussed earlier, long-range pile-up stresses develop within the PSB due to the pile-up of dislocations at the intersection of PSB-GB. Schouwenaars et al. calculated the average of the stress fields of pile-ups with randomly distributed numbers of dislocations [50]. For such a stress field which has a non-zero average stress, they derived an expression for the maximum value of the pile-up stress and showed that it would increase linearly with accumulated slip system strain during incipient deformation, and in addition showed, that it is independent of the grain size. We adapt their formulation of pile-up stress into our continuum definition of pile-up stress (Eq. (15)) and calculate it by obtaining the accumulated slip system strain, γ^{α} , for the most active slip system already determined (as described in Section 3.2.1).

High stress and displacement fields developed due to the pileup of dislocations at the PSB-GB intersection trigger cracks to nucleate. Hence it is worthwhile to study the stress-fields due to a pile-up of dislocations and the associated displacement fields, which present an opening length-scale to promote a crack to nucleate. For this purpose, a dislocation pile-up was considered with twenty edge-dislocations, with their Burgers vector pointing in X-direction, while the dislocation line direction pointed in the Zdirection, as shown in Fig. 6a. Hence from the elastic description of edge-dislocations, the strain and the displacement fields in the Zdirection are zero. This makes it a plane strain problem in the XY plane. For the plot in Fig. 6, the material is assumed isotropic for this analysis and image forces at the GB are not considered in calculating the equilibrium positions of dislocations. For this setup we calculated the equilibrium positions of dislocations in a pile-up subjected to a resolved shear stress of 100 MPa. The stress field σ_{YY} and the displacement-field U_{yy} were plotted to understand the driving forces for crack opening along the YY direction. The stress-field, σ_{YY} , around an edge dislocation is given by Ref. [55]:

$$\sigma_{YY} = \ \frac{-\mu b}{2\pi (1-\nu)} \frac{y \big(x^2-y^2\big)}{(x^2+y^2)^2}. \eqno(21)$$

The displacement-field, U_{yy} , around an edge dislocation is given by Ref. [56]:

$$U_{yy} = \frac{b}{2\pi} \left(\frac{1 - 2\nu}{2(1 - \nu)} \ln \frac{1}{\sqrt{x^2 + y^2}} + \frac{1}{2(1 - \nu)} \frac{y^2}{x^2 + y^2} \right). \tag{22}$$

The stress and displacement fields due to the dislocation pile-up are shown in Fig. 6b and c. It can be observed that the stress field at the intersection of the pile-up and the GB is at its peak, whereas the peak of the displacement field is slightly offset from the pile-up and GB intersection, possibly leading us to insights on why cracks initiate at a slightly offset distance from the TBs, rather than at the TBs [19,21]. Significant work-hardening occurs within the PSB and evolves within the PSB according to the Taylor hardening relation [57] given by:

$$\sigma_{hardening} = 0.45 \mu b \sqrt{\rho}, \tag{23}$$

where ρ is the dislocation density within the PSB.

3.3. Crystal plasticity finite element (CPFE) framework

Crystal plasticity forms a bridge between applied macroscopic load and micro-mechanical response at a slip-system level. The CPFE framework combines anisotropic elasticity with rate dependent crystal plasticity kinetics. It must be noted that inelastic deformation is not only a result of crystallographic slip, it may also occur via twinning, diffusion, and GB sliding. In the current framework, plastic flow occurs primarily through dislocation glide, at the temperature of interest (e.g., an intermediate elevated)

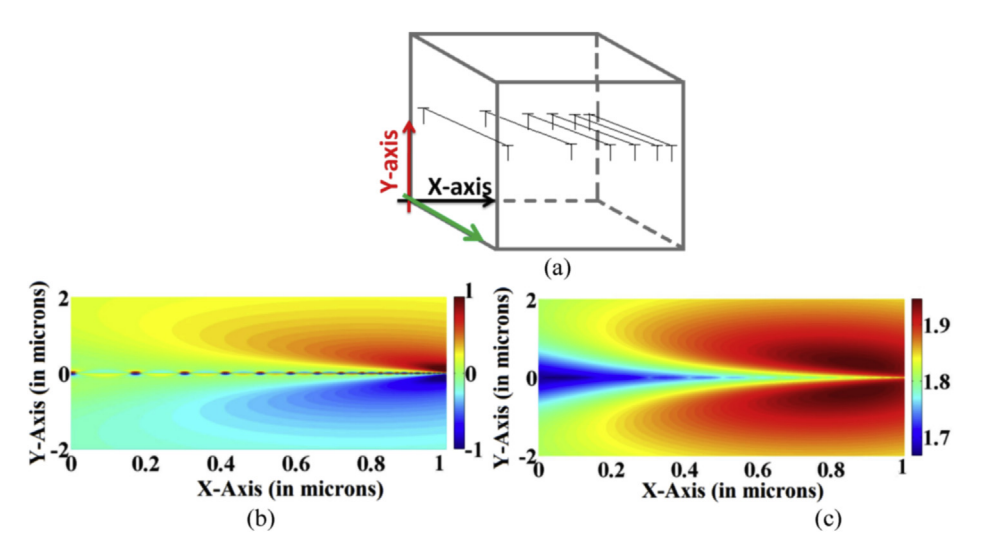


Fig. 6. (a) Coordinate system of the pile-up, (b) σ_{yy} field due to the pile-up (units of the stress are in GPa), and (c) U_{yy} displacement field due to the pile-up (units of displacement are in nm).

temperature).

The values of independent cubic elastic constants, C_{ij} , are used to solve for anisotropic elastic response of the polycrystalline nickelbase superalloy, RR1000. As the γ' phase is not being explicitly modeled, the C_{ij} values are homogenized using the first order Voigt–Reuss–Hill (VRH) method [58] as follows:

$$C_{ij} = 0.5 \Biggl(f C_{ij}^{\gamma'} \ + \ (1-f) C_{ij}^{\gamma} \ + \ \frac{C_{ij}^{\gamma} C_{ij}^{\gamma'}}{f C_{ij}^{\gamma'} \ + \ (1-f) C_{ij}^{\gamma}} \Biggr), \eqno(24)$$

where f is the volume fraction of the γ' phase and C_{ij}^{γ} represent elastic constants of Ni and $C_{ij}^{\gamma'}$ represent the elastic constants of γ' phase. Kuhn et al. [58] showed that the difference between the simpler first-order rules (like the VRH rule) and higher-order structure-property rules (which take into account volume fraction, shape, orientation, and orientation distribution of a second phase) for a material containing globular γ' precipitates is less than 1% and hence justified the use of VRH rule to calculate homogenized elastic constants for nickel-base superalloys.

In RR1000, the volume fraction of γ' phase is 48% [59]. The $C_{ij}^{\gamma'}$ and $C_{ij}^{\gamma'}$ values of both the phases at the intermediate temperature of interest, are taken from literature [60,61]. The elastic constants obtained from VRH method gave a very close value for the Young's modulus when a virtual microstructure was subjected to an elastic strain, however there was still 5% error, when compared to the experimental value. Hence the values of C_{ij} were adjusted using a binary search method, during which the C_{ij} values were adjusted until the Young's modulus value matched accurately with the experimental value. The final C_{ij} values obtained are as follows:

$$C_{11} = 234.52 \; \text{GPa}, \; C_{12} = 130 \; \text{GPa}, \; C_{44} = 103 \; \text{GPa}$$

The flow rule describing incremental slip system strain is adapted in this framework:

$$\dot{\gamma}^{\alpha} = \dot{\gamma}_{0} \left| \frac{\tau^{\alpha} - \chi^{\alpha}}{g^{\alpha}} \right|^{m} sgn(\tau^{\alpha} - \chi^{\alpha}), \tag{25}$$

where $\dot{\gamma}^{\alpha}$ is the shearing rate of slip-system α , $\dot{\gamma}_{0}$ is the reference shearing rate, τ^{α} , χ^{α} , g^{α} are the corresponding slip system shear stress, back stress (that accounts for Bauschinger effects) and critical resolved shear stress (or slip resistance which delays the onset of plastic deformation), respectively. The slip resistance and back stress evolve according to an Armstrong–Frederick hardening model [62]:

$$\dot{g}^{\alpha} = H \sum_{\beta=1}^{N} q^{\alpha\beta} \left| \dot{\gamma}^{\beta} \right| - R g^{\alpha} \sum_{\beta=1}^{N} \left| \dot{\gamma}^{\beta} \right| \tag{26}$$

$$\dot{\chi}^{\alpha} = c\dot{\gamma}^{\alpha} - d\chi^{\alpha}|\dot{\gamma}^{\alpha}|, \tag{27}$$

where H and R are the direct hardening and dynamic recovery coefficients, respectively, for the isotropic hardening relation (Eq. (26)) and c and d are the direct hardening and dynamic recovery coefficients, respectively, for the non-linear kinematic hardening relation (Eq. (27)), $q^{\alpha\beta}$ refers to hardening coefficient for interaction between slip systems, and is assigned a value of 1 (for self-hardening) and 1.2 (for latent-hardening).

There are a total of nine fitting parameters in the CPFE framework. The effect of each of the parameters on the macroscopic response was determined by doing sensitivity analysis, after which the parameters were fit to match the stress—strain curve response to that of the experimental macroscopic response for the first

fatigue cycle (along with the response pertaining to tenth cycle and half-life), as shown in Fig. 7.

It is not computationally feasible to run thousands of fatigue cycles using CPFE framework. Further, crystal plasticity cannot capture the formation of PSBs within the microstructure for the following two reasons. First, all the grains (within the SEM) are idealized by assigning a uniform orientation at every material point (or integration point) and homogenizing the response of the γ' precipitates, due to which, the orientation gradient and shearing of γ' precipitates required to capture the PSB is lost. Second, the mesh size assigned to the volume mesh of the SEMs is on the order of a few microns, whereas the width of PSBs is on the order of tens to hundreds of nanometers. Reducing the mesh size to capture individual PSBs would increase the computational time by at least two orders of magnitude, thereby making it not amenable to carry out CPFE simulations. Hence we only simulate one fatigue cycle and leverage the resulting micromechanical data (RSS, normal stress, critical resolved shear stress, back stress, active slip systems, etc.) within the PSB model.

3.4. Integration of the fatigue model and CPFEM

From the previous discussion, it is clear that the PSB energy formulation needs slip-system level information like the resolved shear stress $(\Delta \tau_{CPFEM}^{\alpha})$, normal stress (σ_{N}^{α}) , critical resolved shear stress (g^{α}) , back stress (χ^{α}) , and accumulated plastic strain (γ^{α}) over the slip system on which the PSB forms. Apart from these quantities, the F^{e-1} tensor and effective accumulated plastic strain (p) at all the material points is also extracted to study the hot-spots (crack initiation sites predicted by the PSB energy based failure model) in detail. All the aforementioned parameters are called the state dependent variables (SDVs). In addition to the SDVs other geometrical information pertaining to the PSB (including its length, L, assuming that the PSB passes through the centroid of the grain along the slip system with maximum RSS) is also extracted from the surface mesh of the SEM. The SDV information $(\Delta \tau_{CPFEM}^{\alpha}, \ \sigma_{N}^{\alpha}, \ \chi^{\alpha}, \ g^{\alpha}, \ \gamma^{\alpha}, \ p, \ F^{e-1})$ from all the material points in every grain are extracted using an ABAQUS-Python interface. As it is

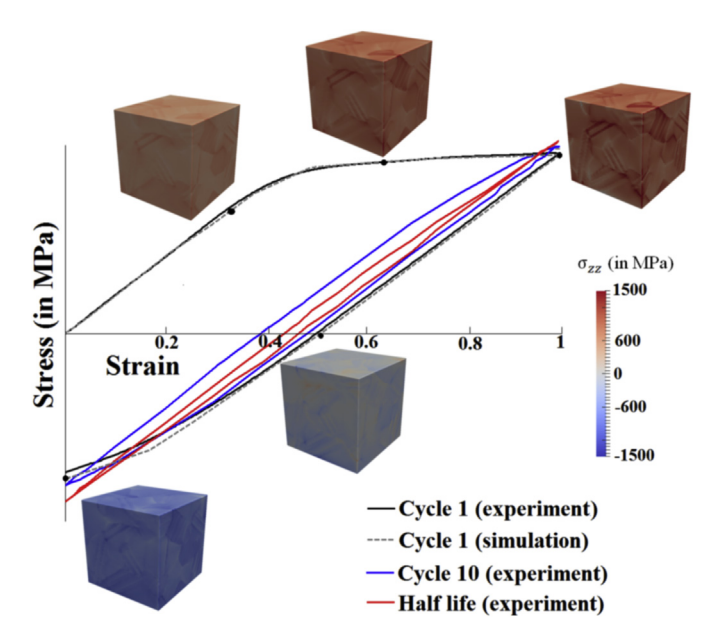


Fig. 7. The macroscopic curve obtained by fitting the parameters to match the experimental macroscopic stress—strain curve. The inlets show contour plots of stress component in the loading direction.

assumed that the PSB forms on an active slip system with the highest resolved shear stress, in every grain the most active slip system is determined based on the maximum resolved shear stress criterion, as discussed in Section 3.2.1. For this slip system the normal stress, critical resolved shear stress, back stress and the accumulated stain are also calculated.

For the sake of simplicity, it is also assumed that the PSB passes through the centroid of the grain. The length of the most active slip system passing through the centroid of the grain is calculated, by determining the two facets (in the surface mesh of the grain) on which the PSB would intersect and then finding the distance between the two intersection points. If the grain forms a cluster of grains joined by LAGBs (as shown in Fig. 2), the lengths of the PSBs in individual grains comprising the cluster are summed. Thus the geometric and the state variable information pertaining to the most active slip system on which the PSB formed (in grains or cluster of grains) is calculated and is fed into the PSB model. The flowchart in Appendix A shows the framework of the fatigue model that begins from statistical characterization of real material's microstructure to the prediction of hot-spot within the SEM.

4. Results and discussion

A representative volume element (RVE) encompasses a large enough volume that is representative of the material as a whole such that the predicted responses or properties do not change with a further increase of size [63,64]. Although by definition, an SEM is not related to the response of the material, with an increase in its volume, it can accurately capture a material response (or property) of interest, and hence, it can attain the essence of an RVE. In practice, the size of an RVE depends on the material response of interest. For instance, the size of an RVE to predict elastic modulus of a material is much smaller compared to the size of an RVE required to accurately predict fatigue life [64]. The scope of the current work is not to determine an RVE which captures all the extreme value statistics of fatigue crack initiation, as such an RVE contains thousands of grains, making it a challenge to run computationally intensive CPFE simulations.

The fatigue framework simulates the microstructure variability by using many number of SEMs generated via Monte-Carlo algorithms in DREAM.3D, which takes into account, the statistical attributes of the real microstructure (as discussed in Section 2). Taking this as leverage, we generate many unique SEMs, which are randomly sampled populations of location specific microstructures within the component. We note that each of these samplings is independent. Although SEMs are small volume elements compared to an RVE, in this study, they are made sufficiently large to capture distributions of microstructural attributes (grain size, GB character, etc.) in addition to strength properties (elastic modulus, yield stress, hardening response and reverse plasticity upon unloading) of the material. Accordingly, a SEM in our work can be regarded as an RVE for the microstructural attributes and strength properties, but not for assessing the minimum fatigue life of the material. To capture the aforementioned properties, a SEM encompassing a minimum volume of $160 \times 160 \times 160 \,\mu\text{m}^3$ and consisting of at least 150 grains serves as an RVE, which is in agreement with the estimation of Lin et al. [65], who defined the size of an RVE (for strength properties) for RR1000. These SEMs were created as per the schematic shown in Fig. 1, by first generating a parent microstructure having roughly around 50 grains (without twins), and then inserting 60 twins (making sure that no twins are inserted in parent grains which are already small, with grain sizes less than 10 µm) in such a way that the average grain size and the percentage of twins in SEMs match that of the real microstructure. For each individual SEM, the fatigue model deterministically calculates fatigue life on a grain-by-grain basis, assuming that a PSB already exists on the most active slip system on every grain. By using multiple SEMs, thousands of grains can be probed by the fatigue model to obtain their respective fatigue lives. The resulting is pooled together to get a fatigue life distribution, in order to connect variability in microstructure to scatter in fatigue life.

In order to study the effect of the size of an SEM on the fatigue life distribution curve, three populations of SEMs were generated. with the first population consisting of 15 SEMs with 100 grains each, second population consisting of 10 SEMs with 150 grains each, and third population consisting of 7 SEMs with 200 grains each, in order to ensure a similar quantity of grains within each population. It is noteworthy to point out that as the size of an individual SEM increases (going from 100 grain to 200 grains), it attains the ability to capture the higher order moments of grain size distribution (skewness and kurtosis) in addition to capturing the lower order moments (mean and variance), which in turn enables a more appropriate analysis of those material responses that are specifically dependent on the extreme value attributes [66], for instance, the fatigue life [64]. Three fatigue life distribution curves at an applied strain range of 1.0% were created (as shown on a log-log plot in Fig. 8), one for each population of SEMs, by pooling the fatigue lives obtained by probing the PSB model through all grains (or grain clusters) in a given population of SEMs. The values for the number of cycles to failure are reported on a normalized scale, as a ratio of the maximum predicted number of cycles to failure. The fatigue life distribution curve obtained from the third population of SEMs (with 200 grains in each SEM) captures the most conservative fatigue life due to the aforementioned reasons. The fatigue life distribution curve obtained from the second population of SEMs (with 150 grains in each SEM) for the most part overlays the third population's fatigue life distribution curve, but is less conservative in nature. Finally, the fatigue life distribution obtained from the first population of SEMs (with 100 grains in each SEM) is farther away from the other two fatigue life distribution curves, and thereby reflecting on the fact that using SEMs with 100 grains is not appropriate to capture fatigue scatter. It is worthwhile to mention that the difference in the least fatigue life obtained by using the second and third population of SEMs is only a few cycles (approximately two orders of magnitude less than the scatter observed from experimental fatigue life data). We can capture the extreme minimum value for fatigue life data by using the population of SEMs with larger number of grains. But capturing the absolute minimum fatigue life data point is not the scope of the current research, as that would require us to define an RVE large enough to capture the least possible fatigue life. The current work focuses on capturing the scatter in fatigue life by simulating the variability in microstructure. Using SEMs with 200 grains in CPFE framework (to obtain the response for one fatigue cycle) takes more than twice the amount of time to simulate SEMs with 150 grains. Hence in order to reduce the computational time, while still being able to capture the scatter in fatigue lives to a reasonable level of accuracy, we use SEMs with at least 150 grains (which captures the microstructure attributes and strength properties), in order to obtain fatigue life distribution and link variability in microstructure to fatigue scatter.

After determining that each SEM needs to have at least 150 grains, we probe the PSB model through 15 unique SEMs and obtain the fatigue life of the hot-spot grain (the one with the least number of cycles to crack initiation) from each SEM at an applied strain range of 1.0%. Hence, we associate each unique SEM with a fatigue life data point and obtain 15 fatigue life predictions from 15 independent SEMs. The fatigue life predictions, thus obtained, are overlaid on a 95% confidence interval plot generated from experimental fatigue life data, as shown in Fig. 9. The values for the

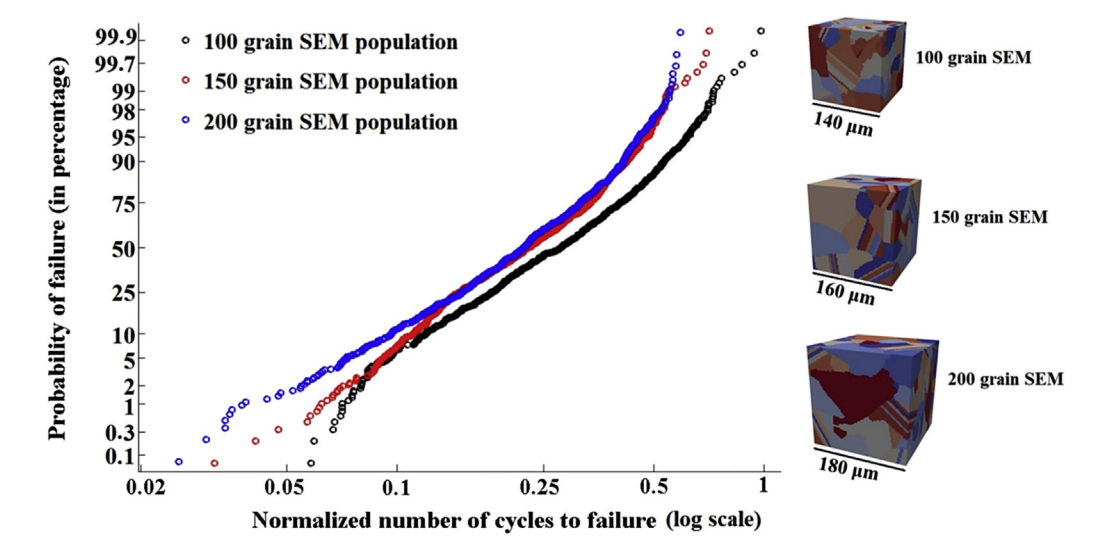


Fig. 8. Effect of the size of an SEM on the fatigue life distribution curve, at an applied strain range of 1.0%. Three SEMs, each taken from three different populations of SEMs, are shown in the inlets. The number of cycles to failure (log scale) is normalized by the maximum predicted value.

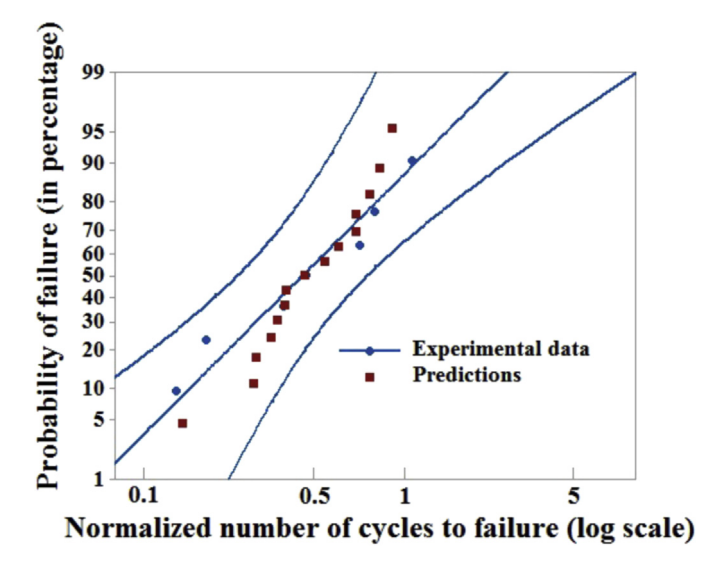


Fig. 9. Fatigue life predictions at an applied strain range of 1.0% obtained by considering fatigue lives of the hot-spot grains (those with the least fatigue lives compared to all other grains) in 15 different SEMs. Predictions from the model are overlaid on the 95% confidence interval plot generated from experimental data. The number of cycles to failure (log scale) is normalized by the maximum experimental value.

number of cycles to failure are normalized by the maximum experimental value. The scatter in the fatigue life predictions obtained (by varying the microstructure) is in good agreement with the scatter observed in experimental fatigue life data. The heterogeneous deformation state of the local microstructure of a hot-spot provides insights about what caused failure at those specific locations. As discussed earlier, the influence of elastic anisotropy and plastic strain accumulation at the hot-spots provides an explanation into the underpinning mechanism of crack nucleation.

Lattice incompatibility develops near GBs as a result of geometric differences in slip system alignment between two neighbors of distinctly different grain orientation. Stress concentrations develop at grain boundaries with high lattice incompatibility. Hence the amount of incompatible stresses can be understood by quantifying lattice incompatibility. For this purpose, we note a tensorial parameter, which by itself cannot describe compatible

deformation. The deformation gradient, $F = F^e F^p$ [54], can define compatible deformation, which is not fulfilled by F^e or F^p alone. Acharya and Beaudoin [67] used F^{e-1} to measure incompatibility as follows:

$$\Lambda \ := \Big(F_{ij,k}^{e-1} - F_{ik,j}^{e-1}\Big)e_i \otimes e_j \otimes e_k, \tag{28} \label{eq:28}$$

where $\{e_i\}$ is the basis of a rectangular Cartesian coordinate system. As the lattice incompatibility developed at the GBs gives rise to incompatible stresses, we treat the incompatibility, Λ_{eq} , as an equivalent stress metric to study the high elastic anisotropy at the GBs as follows:

$$\Lambda_{\text{eq}} = \left(\frac{3}{2}\Lambda : \Lambda\right)^{\frac{1}{2}}.\tag{29}$$

As previously discussed, strain localization is a precursor to crack initiation. Crystal plasticity framework enables us to quantitatively understand the microstructure dependent evolution of the plastic strain. Effective plastic strain accumulation, p [68], at a material point has been used, in order to study the strain localization in the hot-spots predicted by the PSB model. It is calculated from the plastic velocity gradient $(L_{\rm p})$ as follows:

$$L_p = \dot{\gamma}^{\alpha}(s^{\alpha} \otimes m^{\alpha}), \tag{30}$$

$$\dot{p} = \left(\frac{2}{3}L_p : L_p\right)^{\frac{1}{2}},\tag{31}$$

$$p = \int_{0}^{t} \dot{p} dt, \tag{32}$$

where $\dot{\gamma}^{\alpha}$, s^{α} and m^{α} are the rate of slip, slip direction and the slip plane normal of the slip system α , respectively.

As a visual example, for the three hot-spots that display the lowest lives (in three different SEMs) based on the PSB model's predictions, the elastic anisotropy (Λ_{eq}) and plastic strain accumulation (p) were plotted over all the material points within the respective SEMs (Fig. 10) at maximum applied macroscopic strain (or at the end of the one fatigue cycle simulated in CPFE). In

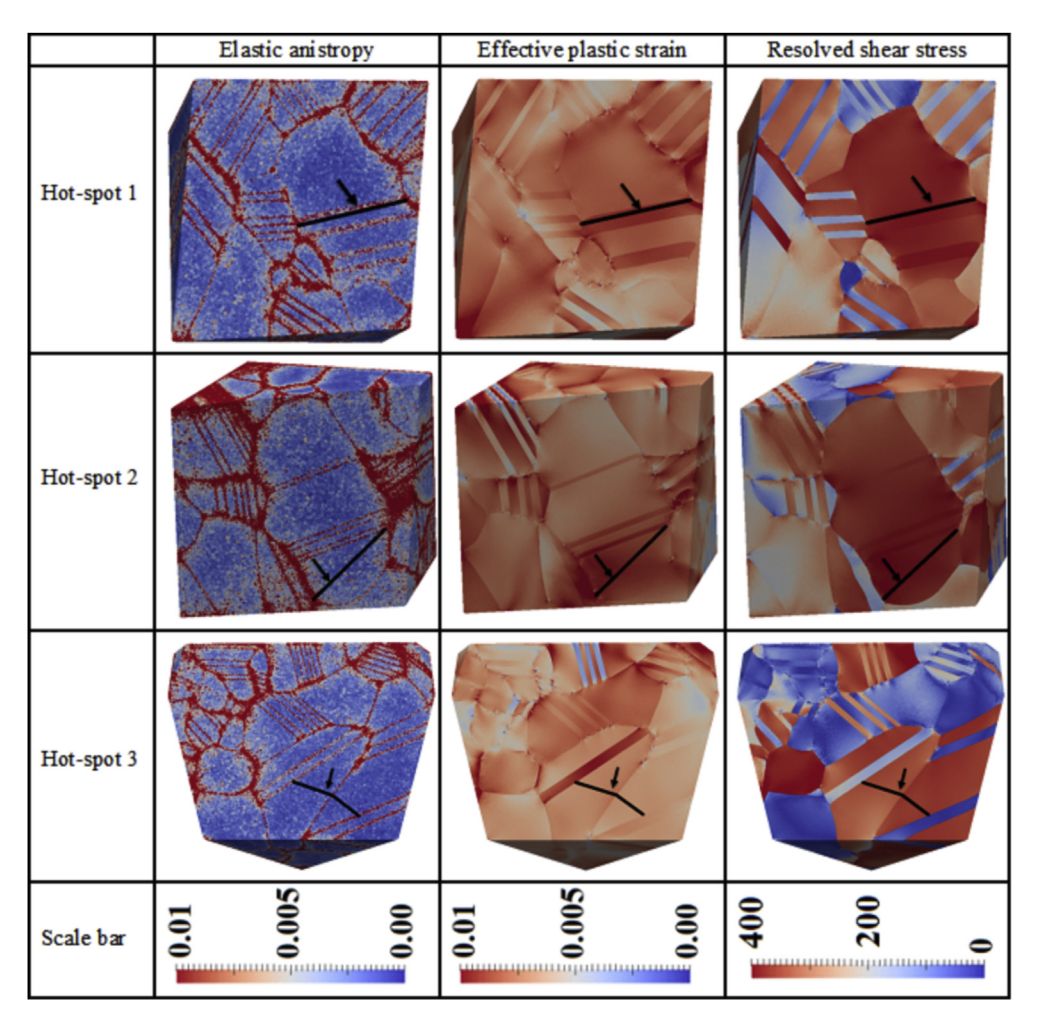


Fig. 10. A cross-sectional plane through the hot-spots within a SEM to show the elastic anisotropy and plastic strain accumulation fields in the local neighborhood of the hot-spots. In all the plots, the plane passes through the centroid of the hot-spot (grain or cluster of grains) and its normal is parallel to the slip plane normal of the active slip system containing the PSB, shown with a black line and indicated by an arrow. It must also be noted that RSS plots are created on the same slip system (at all material points) based on the slip system on which the PSB formed in the hot-spot grain. Elastic anisotropy (Λ_{eq}) (units $\frac{1}{\mu m^2}$), Plastic strain accumulation (p), RSS (units MPa) are shown at hot-spot 1 (first row), hot-spot 2 (second row) and hot-spot 3 (third row), with the respective scale bars shown in the last row.

addition to those two metrics, the absolute RSS values of that slip system containing the PSB is also plotted. For example, if the PSB formed on slip system 6 within the hot-spot grain (or grain cluster), then the absolute RSS values of slip system 6 at all material points in the SEM are plotted for mere comparison purposes. In order to visualize the PSB alignment, the local anisotropy, and strain accumulation, a plane section is cut through the hot-spot grain along the slip plane containing the PSB and is extended through the SEM. The first row in Fig. 10 shows the elastic anisotropy, plastic strain accumulation, and the RSS plotted over the cross-section of an SEM containing hot-spot 1, the second row in Fig. 10 shows the plots of the three aforementioned metrics over the cut section of an SEM containing hot-spot 2 and similarly, the third row in Fig. 10 shows the plots of the same metrics over the cross-section of a SEM containing hot-spot 3. In all the figures, the PSB slip system is shown with a black line superimposed on the microstructure for clarity. It can be clearly seen that in all the three hot-spots, cracks are predicted to initiate where the PSB is interacting with the TB. Hot-spots 1 and 2 correspond to a PSB forming in a single grain, whereas hot-spot 3 corresponds to a cluster of two grains sharing an LAGB. Further, it can be clearly seen from all the three hot-spots that the PSB model predicts that cracks initiate at a twin boundary embedded in a relatively large grain/grain clusters compared to

small grains, which is in agreement with experiments [19,21].

It can be seen from the elastic anisotropy plots (shown in the first column of Fig. 10) that the value of Λ_{eq} is highest at the GBs, and the TBs, in particular, show high degree of anisotropy. The orientations of all the material points within each grain of the SEM are assigned the same values, hence it is an idealization compared to real materials that display intergranular misorientations and residual stresses. Due to this reason, the elastic anisotropy results are observed to be high only at the GBs and have near zero values away from the GB in the core of the grain. But if we were to model grains with internal rotations with high resolution meshes, the elastic anisotropy of the slip bands can also be observed at the expense of computational time. The plastic strain accumulation however seems to accumulate at the GBs and also varies across the grains.

In all the hot-spots displayed, the elastic anisotropy, plastic strain accumulation, and the RSS have high values, which are partially attributed to a high probability for crack initiation at these material points. High elastic anisotropies can be clearly observed in the vicinity of twins. In addition to that, since TBs are the strongest barriers to slip transmission, dislocations pile-up at twin boundaries [26,27]. In other words, high lattice incompatibility at TBs and the long-range stress field created by dislocation pile-ups at the

TBs, can potentially increase the stress concentrations and lead to crack initiations. This can be a partial explanation for the high probability of crack initiation at TBs as predicted by the PSB model.

Such a detailed analysis of the 3D heterogeneities (in elastic anisotropy and plastic strain accumulation) is only possible by the use of crystal plasticity. Additionally, the use of CPFE helped i) reduce the number of experimental evolution functions and fitting parameters used in the earlier version of the PSB energy balance for U720 [22,27,28] and ii) eliminate the use weakest link theory, by providing more information on the location specific heterogeneous deformation.

As relatively high values of both metrics (Λ_{eq} and p) are observed to occur at the GBs, average values of both the metrics are calculated at the GBs for every grain within an SEM. This information is linked with the fatigue lives calculated for all the grains. Based on this accumulated data, a response surface (shown in Fig. 11) is constructed. It can be clearly visualized that lower values for fatigue lives are observed for grains that have extreme values of elastic stress anisotropy and plastic strain accumulations at the GBs.

Critical life limiting parameters like elastic anisotropy, accumulated plastic strain, and maximum RSS are conditions that must be satisfied to identify certain microstructural features exhibiting a high probability for potential crack nucleation. Hence the evolution of these three parameters was calculated over 10 cycles of strain controlled loading (using a smaller SEM consisting of 100 grains, in order to save a significant amount of computational time in simulating 10 fatigue cycles, while still being able to study the evolution of life limiting parameters). Fig. 12 shows the evolution of these parameters over cycles 1, 2, 5 and 10, with each plot taken at the maximum applied strain over the corresponding cycle. It can be observed that the lattice incompatibility remains consistent during the cyclic loading. The plastic strain accumulation on the other hand shows a clear positive trend in evolution, and it can be explained by the fact that low cycle fatigue regime results in incremental plastic strain accumulation per cycle. At the microstructure level, this leads to more dislocation pile-ups at the GBs. From Fig. 10, annealing TBs accumulate high strains with an increase in cyclic loading. This observation provides insights as to why TBs are preferred locations for cracks to initiate. Maximum RSS calculated at every material point in the SEM also shows a similar incremental trend, which can be attributed to the increased hardening observed with cyclic loading. High values of maximum RSS observed at TBs are a result of high elastic anisotropy and strain accumulation.

While elastic stress anisotropy and plastic strain accumulation along with the RSS play an important role by acting in concert to

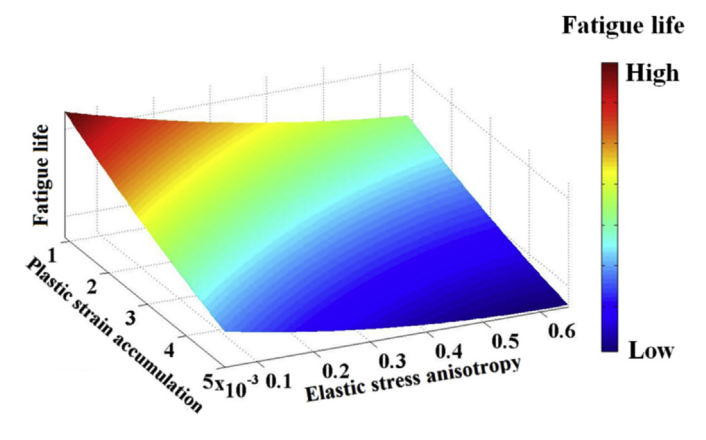


Fig. 11. Influence of elastic stress anisotropy and plastic strain accumulation on fatigue life.

initiate fatigue cracks, normal stress also has a significant role to play in limiting fatigue life of the material. With this as a motivation, in classical fracture mechanics terms, the crack driving force can be promoted by either mode I initiation based on the normal tensile stress along the twin boundary or mode II initiation based on the resolved shear stress along the twin boundary. Due to the propensity of fatigue crack initiation in the vicinity of favorable oriented TBs with long slip traces, it is worthwhile to study the synergistic/competing role played by the RSS and the normal stress (acting on the twin boundaries). For this purpose, we further analyze the stress state of hot-spot 1 (shown in the first row of Fig. 10), which is one of the twin lamellae (inside a large grain) encompassing a PSB. The values of the RSS (for the slip system corresponding to the PSB) and normal stress (acting perpendicular to the slip plane containing the PSB) are obtained at every integration point within the twin (at the peak applied macroscopic load), and their cumulative distributions are plotted (as shown in Fig. 13). Over a majority proportion of the volume within the twin, the normal stress was observed to dominate the RSS, which suggests a significant role played by the normal stress in unzipping a PSB at the intersection of the twin boundary to act as a mode I

Further, a cumulative distribution obtained by pooling together the absolute values of the RSS for all the 12 slip systems in the grain is compared to the RSS corresponding to the PSB's slip system. A considerable amount of scatter is observed in the former, compared to the latter (which has a uniformly high RSS within the PSB). The same is not true in the case of normal stress, which has significantly higher values on certain locations of the grain, as shown in the inlets of Fig. 13. Thus, the highest value of normal stress is observed at the PSB-twin boundary intersection, resulting in a normal tensile stress to open a crack along the twin boundary.

Due to strain controlled loading applied on the SEM with a constant strain range in every cycle (as shown in Fig. 14a), it was observed that the difference in strain accumulation between the fully loaded states of any two consecutive cycles remains almost the same (Fig. 14b). Although crystal plasticity accounts for cyclic hardening to an extent, it cannot capture the cyclic slip irreversibilities that arise from defect level deformation mechanisms. Hence, crystal plasticity by itself is not sufficient to model fatigue and predict life. Due to a similar trend in the evolution of the stress/strain states with increasing number of cycles, we take the output from CPFE simulations over one fatigue cycle and leverage this data as input into the PSB model, which also considers slip irreversibilities.

Slip in cyclic loading is distinguished from that of monotonic loading. During forward and reverse loading, the material undergoes irreversible slip, which leads to distinct defect structures [3-5]. To date, the majority of the computational fatigue models attempt to use the same tools to model cyclic and monotonic loading, albeit these models exhibit limited success since they cannot capture the complex and unique features of the fatigue phenomena. Various forms of cyclic slip irreversibilities manifests during cyclic loading in polycrystalline materials and their contributions to the fatigue damage evolution is inherent within the present fatigue model. Cyclic slip irreversibilities are the fraction of plastic shear strain that is microstructurally irreversible [10]. These irreversibilities can occur both on the surface and in the bulk of the material [6]. Irreversibilities on the surface cause roughness, due to accumulation of slip steps. In the bulk of the material irreversibilities occur due to i) dislocations becoming sessile due to the formation of locks that impede subsequent dislocation glide, ii) annihilation of positive and negative dislocations, iii) slip-GB interaction which leaves a residual Burgers vector within the GB causing extrusions to grow with repeated loading, iv) shearing of

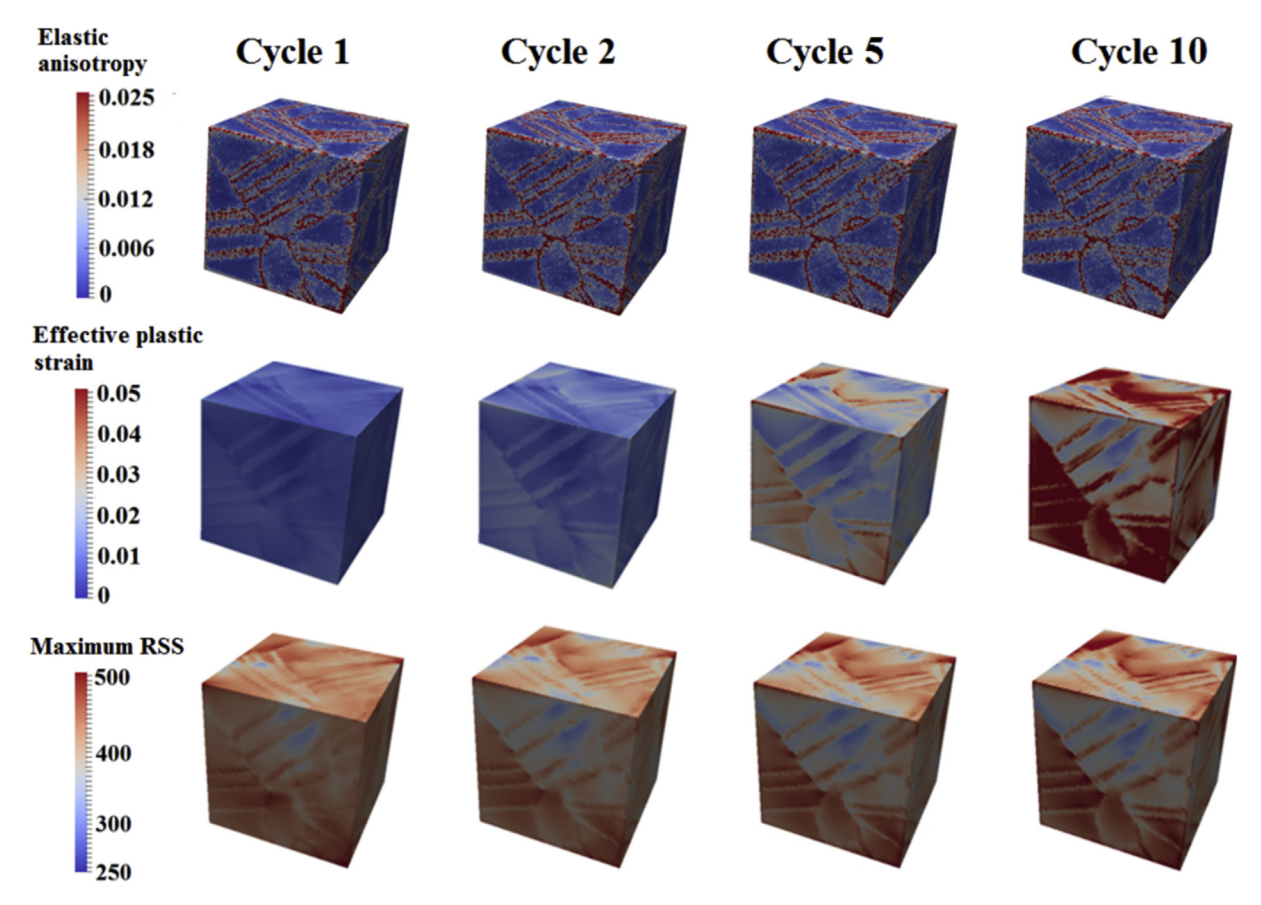


Fig. 12. Evolution of elastic anisotropy (Λ_{eq}), plastic strain accumulation (p) and maximum resolved shear stress (calculated at every material point over 10 cycles).

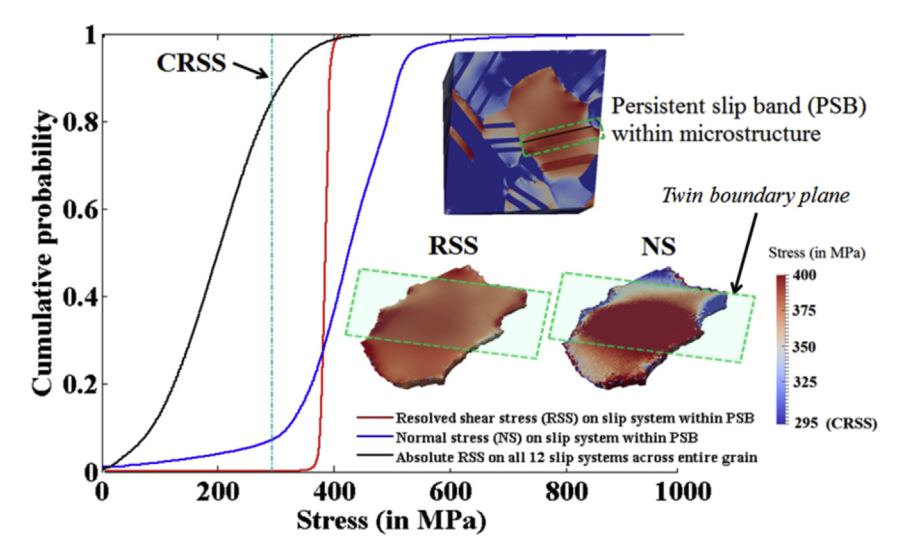


Fig. 13. Cumulative probability distributions of the resolved shear stress (RSS) and normal stress (NSS) at all integration points within the slip system of the critical PSB, along with the RSS values obtained for all slip systems across the entire grain. The critical resolved shear stress (CRSS) is shown as a reference value (with respect to slip system activation). The inlet figures show (top) an RSS plot on the cross-section view of the SEM and (bottom) contour plots of the RSS and NS values over the slip system corresponding to that of the PSB.

the precipitate, and v) dislocation climb at high temperatures [6,7,10,13]. These defect level mechanisms can be accounted for, by calculating the activation energy required for each process to occur. Since the current fatigue model is an energy-based model, the energies for pertinent dislocation mechanisms contributing

towards irreversibilities are calculated, specifically shearing of precipitates, formation of unique dislocation arrangements within PSBs, and development of extrusions/intrusions at GBs.

In nickel-base superalloys, a prominent deformation mechanism at intermediate temperatures is through the shearing of the

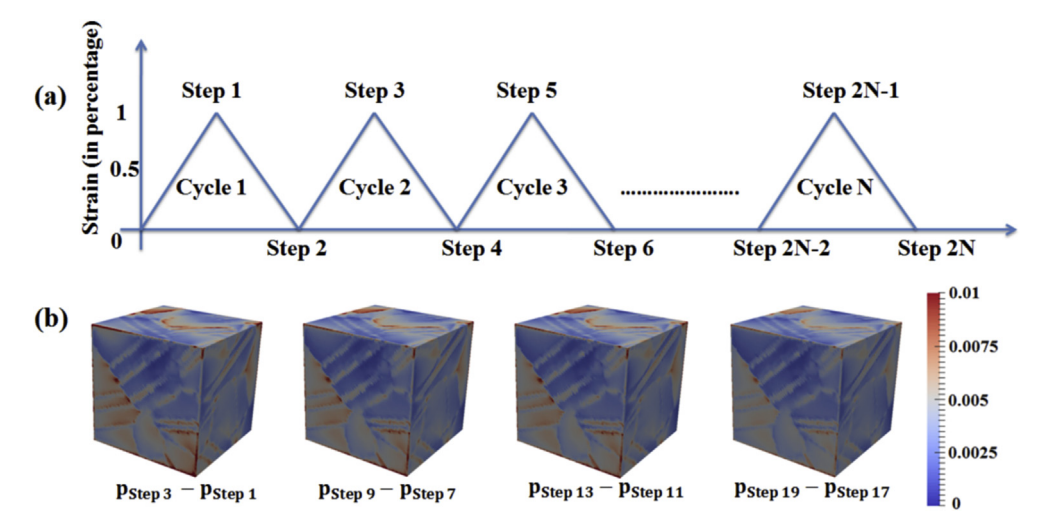


Fig. 14. (a) A strain loading schematic showing the nomenclature of steps and cycles used in the discussion. (b) The difference of effective accumulated plastic strain (p) evaluated at the two consecutive loaded steps, $p_{\text{step } 2N-1}$ and $p_{\text{step } 2N-3}$ corresponding to cycles N and N-1 respectively.

precipitates. Due to intense cyclic slip localization in the PSBs, dislocations are able to shear through the precipitates. The ease at which the precipitates can be sheared depends on the normal strain, work-hardening, and temperature. For instance, as depicted in Fig. 3, a tensile normal strain acting on atomic slip planes will increase the distance between the slip planes which in turn makes it easier for slip to occur thereby reducing the SFE (or APBE) and vice versa. The shearing through precipitate (and matrix), with its dependence on normal strain was taken into consideration using APBE (and SFE) energies obtained from MD simulations (as shown in Fig. 4a and b). Moreover, the energy balance is built for a PSB, which develops unique dislocation arrangements, including dislocation dipoles, as a form of slip irreversibilities. Another contribution to irreversible plastic flow comes from the formation of extrusions from PSB impingement on a HAGB. These extrusions grow in length during cyclic loading due to an increased number of residual dislocations accumulating within the GB [46]. The model takes into consideration the development of extrusions and the associated energy required to form the extrusion [26]. Thus, the cyclic slip irreversibilities due to fatigue are considered into the model by considering the energies required for the fatigue related defect level mechanisms that introduce irreversible plastic flow in the material. The underpinning physics improves the fidelity of the model in investigating the microstructure's role in fatigue crack initiation and also helps link fatigue scatter to variability in the microstructure by sampling many statistical equivalent realizations of defect-microstructure interactions.

5. Conclusions

A microstructure based fatigue framework is developed, which takes into account i) the statistics of the material's microstructure, ii) quantitative input from the complex 3D stress and strain heterogeneities output from CPFE simulations and iii) GB energies calculated from MD simulations to differentiate the role of the GB character. To summarize, the conclusions from the current research work are as follows:

 A microstructure and deformation mechanism based formulation is used to define the energy of a PSB, using the quantitative information obtained from i) continuum scale CPFE simulations which solve for complex 3D stress and strain heterogeneities within the microstructures and ii) atomistic scale MD simulations which provide energies of various types of GBs and defect level mechanisms.

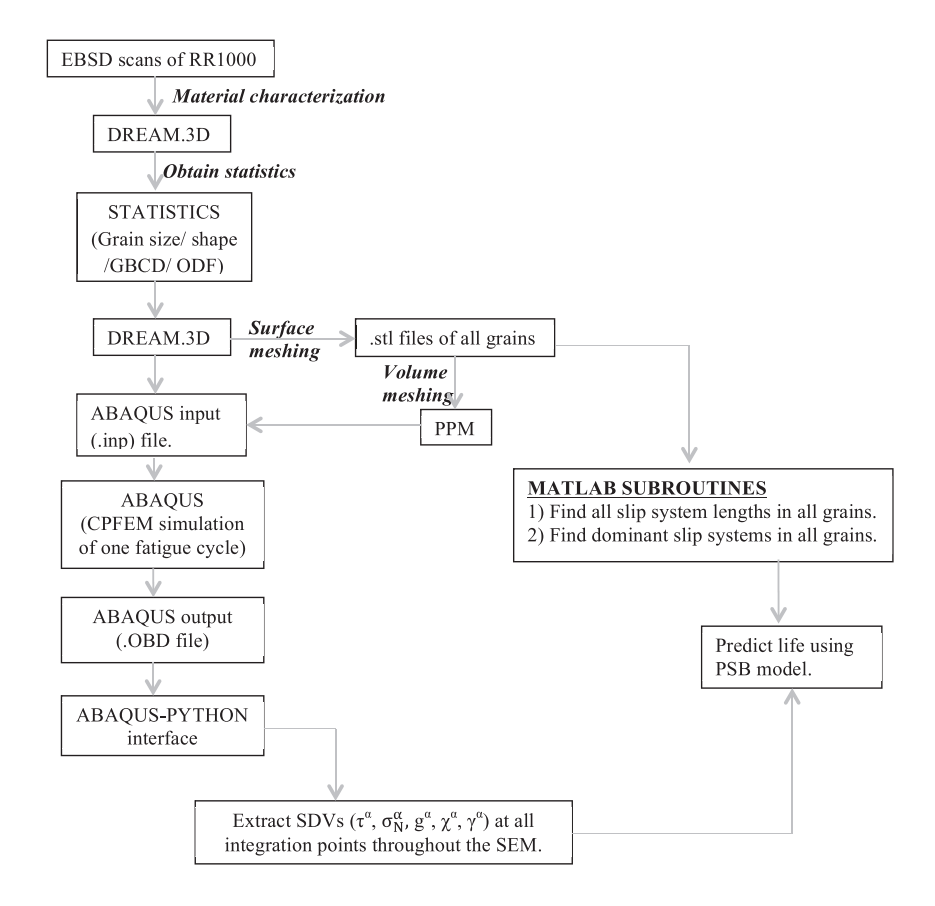
- The significant effect of the normal strain on fatigue life is incorporated into the model by calculating its relationship with the APBE and SFE energies, which contribute to the energy of a PSB.
- The fatigue framework predicts crack initiation to occur at a twin boundary, in a nickel-base superalloy, which is in agreement with experimental observations.
- A high concentration of elastic stress anisotropy and accumulated plastic strain is observed in the immediate vicinity of the twin boundaries where cracks were predicted to initiate.
- Significant normal stress was observed to act on a favorably oriented twin (embedded in a large grain) where cracks were predicted to initiate, such high normal stresses act as a crack driving force.
- Scatter in fatigue life is linked to the microstructure variability, which is simulated by generating multiple statistically equivalent microstructures (with explicitly inserted annealing twins), based on statistics obtained from the real microstructure of the material.
- Fatigue life predictions obtained are in good agreement with experimental data.

Acknowledgments

Support for this work was provided primarily by Rolls-Royce Corporation and partially by the National Science Foundation (CMMI 13-34664). We thank J. Matlik, R. Goetz, J. Stillinger, C. Argyrakis, and B. Saunders of Rolls-Royce for insightful technical discussions. We would like to thank Michael Jackson, Dr. Michael Groeber and Dr. Joseph C. Tucker for their help with DREAM.3D, and Dr. Anthony D. Rollett for sharing his twin insertion code before it was integrated into DREAM.3D. We would also like to thank Dr. Albert Cerrone and Dr. Jacob D. Hochhalter for sharing their ABAQUS-Python interface based volume meshing code.

Appendix A

(Flowchart showing integration of CPFE with fatigue model)



References

- [1] L.F. Coffin, A study of the effects of cyclic thermal stresses on a ductile metal, Trans. Am. Soc. Mech. Eng. 76 (1954) 931–950.
- [2] S.S. Manson, Behavior of Materials Under Conditions of Thermal Stress, National Advisory Commission on Aeronautics: Report 1170, Lewis Flight Propulsion Laboratory, Cleveland, 1954.
- [3] C.E. Feltner, C. Laird, Cyclic stress-strain response of f.c. metals and alloys-II. Dislocation structures and mechanisms, Acta Metall. 15 (1967) 1633–1653.
- [4] D. Kuhlmann-Wilsdorf, Theory of plastic deformation: properties of low energy dislocation structures, Mater. Sci. Eng. A 113 (1989) 1–41.
- [5] P. Neumann, Low energy dislocation configurations: a possible key to the understanding of fatigue, Mater. Sci. Eng. 81 (1986) 465–475.
- [6] U. Essmann, U. Gösele, H. Mughrabi, A model of extrusions and intrusions in fatigued metals. I. Point-defect production and the growth of extrusions, Philos May A 44 (1981) 405–426
- [7] K. Differt, U. Esmann, H. Mughrabi, A model of extrusions and intrusions in fatigued metals. II. Surface roughening by random irreversible slip, Philos. Mag. A 54 (1986) 237–258.
- [8] R.E. Stoltz, A.G. Pineau, Dislocation-precipitate interaction and cyclic stress-strain behavior of a γ' strengthened superalloy, Mater. Sci. Eng. 34 (1978) 275–284
- [9] H.S. Ho, M. Risbet, X. Feaugas, On the unified view of the contribution of plastic strain to cyclic crack initiation: impact of the progressive transformation of shear bands to persistent slip bands, Acta Mater. 85 (2015) 155–167.
- [10] U. Essmann, H. Mughrabi, Annihilation of dislocations during tensile and cyclic deformation and limits of dislocation densities, Philos. Mag. A 40 (1979) 731–756.
- [11] Z.F. Zhang, Z.G. Wang, Dependence of intergranular fatigue cracking on the interactions of persistent slip bands with grain boundaries, Acta Mater. 51 (2003) 347–364.

- [12] Z.S. Basinski, S.J. Basinski, Fundamental aspects of low amplitude cyclic deformation in face-centred cubic crystals, Prog. Mater. Sci. 36 (1992) 89–148.
- [13] M.D. Sangid, The physics of fatigue crack initiation, Int. J. Fatigue 57 (2013)
- [14] S.D. Antolovich, R.W. Armstrong, Plastic strain localization in metals: origins and consequences, Prog. Mater. Sci. 59 (2014) 1–160.
- [15] R.C. Boettner, A.J. McEvily, Y.C. Liu, On formation of fatigue cracks at twin boundaries, Philos. Mag. 10 (1964) 95–106.
- [16] A.W. Thompson, The influence of grain and twin boundaries in fatigue cracking, Acta Metall. 20 (1972) 1085–1094.
- [17] Z.J. Zhang, P. Zhang, L.L. Li, Z.F. Zhang, Fatigue cracking at twin boundaries: effects of crystallographic orientation and stacking fault energy, Acta Mater. 60 (2012) 3113–3127.
- [18] A. Heinz, P. Neumann, Crack initiation during high cycle fatigue of an austenitic steel, Acta Metall. Mater. 38 (1990) 1933—1940.
- [19] J. Miao, T.M. Pollock, J.W. Jones, Crystallographic fatigue crack initiation in nickel based superalloy Rene 88DT at elevated temperature, Acta Mater. 57 (2009) 5964–5974.
- [20] C.A. Stein, A. Cerrone, T. Ozturk, S. Lee, P. Kenesei, H. Tucker, R. Pokharel, J. Lind, C. Hefferan, R.M. Suter, A.R. Ingraffea, A.D. Rollett, Fatigue crack initiation, slip localization and twin boundaries in a nickel-based superalloy, Curr. Opin. Solid State Mater. Sci. 18 (2014) 244–252.
- [21] O.M.D.M. Messé, J. Lachambre, A. King, J.Y. Buffière, C.M.F. Rae, Investigation of fatigue crack propagation in nickel superalloy using diffraction contrast tomography and phase contrast tomography, Adv. Mater. Res. 891–892 (2014) 923–928.
- [22] M.D. Sangid, H.J. Maier, H. Sehitoglu, An energy-based microstructure model to account for fatigue scatter in polycrystals, J. Mech. Phys. Solids 59 (2011) 595–609.
- [23] Z.R. Wang, H. Margolin, Mechanism for the formation of high cycle fatigue

- cracks at fcc annealing twin boundaries, Metall. Trans. A 16 (1985) 873—880. [24] P. Peralta, L. Llanes, J. Bassani, C. Laird, Deformation from twin-boundary stresses and the role of texture: application to fatigue, Philos. Mag. A 70 (1994) 219—232.
- [25] P. Neumann, Analytical solution for the incompatibility stresses at twin boundaries in cubic crystals, in: Proceedings of the Seventh International Fatigue Congress, Beijing, 1999, pp. 107–114.
- [26] M.D. Sangid, T. Ezaz, H. Sehitoglu, I.M. Robertson, Energy of slip transmission and nucleation at grain boundaries, Acta Mater. 59 (2011) 283–296.
- [27] M.D. Sangid, H.J. Maier, H. Sehitoglu, A physically based fatigue model for prediction of crack initiation from persistent slip bands in polycrystals, Acta Mater. 59 (2011) 328–341.
- [28] M.D. Sangid, H.J. Maier, H. Sehitoglu, The role of grain boundaries on fatigue crack initiation an energy approach, Int. J. Plast. 27 (2011) 801—821.
- [29] G.M. Castelluccio, D.L. McDowell, Effect of annealing twins on crack initiation under high cycle fatigue conditions, J. Mater. Sci. 48 (2012) 2376–2387.
- [30] A. Cerrone, C. Stein, R. Pokharel, C. Hefferan, J. Lind, H. Tucker, R. Suter, A. Rollett, A. Ingraffea, Implementation and verification of a microstructurebased capability for modeling microcrack nucleation in LSHR at room temperature, Model. Simul. Mater. Sci. Eng. 23 (2015) 1–31.
- [31] P. Feltham, Grain growth in metals, Acta Metall. 5 (1957) 97–105.
- [32] M. Groeber, Development of an Automated Characterization-representation Framework of Polycrystalline Materials in 3D (PhD thesis), Ohio State University, USA, 2007.
- [33] M.A. Groeber, M.A. Jackson, January 2016. http://dream3d.bluequartz.net/.
- [34] M.A. Groeber, M.A. Jackson, DREAM.3D: a digital representation environment for the analysis of microstructure in 3D, Integr. Mater. Manuf. Innov. 3 (2014) 1–17.
- [35] L. Chan, Synthetic Three-dimensional Voxel-based Microstructures that Contain Annealing Twins (PhD thesis), Carnegie Mellon University, USA, 2010.
- [36] A. Cerrone, January 2016. http://www.cfg.cornell.edu/~arc247/PPM/ Documentation.html.
- [37] K. Tanaka, T. Mura, A dislocation model for fatigue crack initiation, J. Appl. Mech. 48 (1981) 97–103.
- [38] S. Plimpton, Large-scale Atomic/Molecular Massively Parallel Simulator (LAMMPS), January 2016. http://lammps.sandia.gov/.
- [39] O.M.D.M. Messé, S. Stekovic, M.C. Hardy, C.M.F. Rae, Characterization of plastic deformation induced by shot-peening in a Ni-base superalloy, J. Mater. 66 (2014) 2502–2515.
- [40] S.M. Foiles, J.J. Hoyt, Computation of grain boundary stiffness and mobility from boundary fluctuations, Acta Mater. 54 (2006) 3351–3357.
- [41] Y. Mishin, Atomistic modeling of the γ and γ'-phases of the Ni–Al system, Acta Mater. 52 (2004) 1451–1467.
- [42] A. Fatemi, D.F. Socie, A critical plane approach to multiaxial fatigue damage including out-of-phase loading, Fatigue Fract. Eng. Mater. Struct. 11 (1988) 149–165.
- [43] D.S. Xu, R. Yang, J. Li, J.P. Chang, H. Wang, D. Li, S. Yip, Atomistic simulation of the influence of pressure on dislocation nucleation in bcc Mo, Comput. Mater. Sci. 36 (2006) 60–64.
- [44] M.A. Tschopp, D.L. McDowell, Influence of single crystal orientation on homogeneous dislocation nucleation under uniaxial loading, J. Mech. Phys. Solids 56 (2008) 1806–1830.
- [45] Y. Sun, J.R. Rice, L. Truskinovsky, Dislocation Nucleation Versus Cleavage in Ni₃Al and Ni, Materials Research Society, Pittsburgh, 1991, p. 243.
- [46] T.C. Lee, I.M. Robertson, H.K. Birnbaum, TEM in situ deformation study of the interaction of lattice dislocations with grain boundaries in metals, Philos. Mag. A 62 (1990) 131–153.

- [47] M. Risbet, X. Feaugas, C. Guillemer-Neel, M. Clavel, Use of atomic force microscopy to quantify slip irreversibility in a nickel-base superalloy, Scr. Mater. 49 (2003) 533–538.
- [48] A.N. Stroh, A theory of the fracture of metals, Adv. Phys. 6 (1957) 418–465.
- [49] H.J. Christ, On the orientation of cyclic-slip-induced intergranular fatigue cracks in face-centred cubic metals, Mater. Sci. Eng. A 117 (1989) L25–L29.
- [50] R. Schouwenaars, M. Seefeldt, P. Van Houtte, The stress field of an array of parallel dislocation pile-ups: implications for grain boundary hardening and excess dislocation distributions. Acta Mater. 58 (2010) 4344–4353.
- [51] D.L. Olmsted, S.M. Foiles, E.A. Holm, Survey of computed grain boundary properties in face- centered cubic metals: I. Grain boundary energy, Acta Mater. 57 (2009) 3694–3703.
- [52] T.A. Parthasarathy, S.I. Rao, D.M. Dimiduk, A fast spreadsheet model for the yield strength of superalloys. Superalloys (2004) 887–896.
- [53] R.J. Asaro, A. Needleman, Texture development and strain hardening in rate dependent polycrystals, Acta Metall. 23 (1984) 923–953.
- [54] E.H. Lee, Elastic-plastic deformations at finite strains, J. Appl. Mech. 36 (1969) 1–6
- [55] J.P. Hirth, J. Lothe, Theory of Dislocations, second ed., Wiley, New York, 1982.
- [56] J.D. Eshelby, Simple derivation of the elastic field of an edge dislocation, Br. J. Appl. Phys. 17 (1966) 1131–1135.
- [57] G.I. Taylor, The mechanism of plastic deformation of crystals, Proc. Roy. Soc. 145 (1934) 362–387.
- [58] H.A. Kuhn, H.G. Sockel, Contributions of the different phases of two nickel-base superalloys to the elastic behaviour in a wide temperature range, Phys. Status Sol. A 119 (1990) 93–105.
- [59] M. Preuss, J.Q. Fonseca, B. Grant, E. Knoche, R. Moat, M. Daymond, The effect of γ' particle size on the deformation mechanism in an advanced polycrystalline nickel-base superalloy, in: R.C. Reed, K.A. Green, P. Caron, T.P. Gabb, M.G. Fahrmann, E.S. Huron, S.A. Woodard (Eds.), Superalloys 2008, The Minerals, Metals and Materials Society, 2008, pp. 405–414.
- [60] G.A. Alers, J.R. Neighbours, H. Sato, Temperature dependent magnetic contributions to the high field elastic constants of nickel and an Fe-Ni alloy, J. Phys. Chem. Solids 13 (1960) 40–55.
- [61] S.V. Prikhodko, H. Yang, A.J. Ardell, J.D. Carnes, D.G. Isaak, Temperature and composition dependence of the elastic constants of Ni₃Al, Metall. Mater. Trans. A 30 (1999) 2403–2408.
- [62] P.J. Armstrong, C.O. Frederick, A Mathematical Representation of the Multi-axial Bauschinger Effect, Report RD/B/N, 731, Central Electricity Generating Board, Berkeley, UK, 1966.
- [63] D.L. McDowell, S. Ghosh, S.R. Kalidindi, Representation and computational structure-property relations of random media, J. Mater. 63 (2011) 45–51.
- [64] M.P. Echlin, W.C. Lenthe, T.M. Pollock, Three-dimensional sampling of material structure for property modeling and design, Integr. Mater. Manuf. Innov. 3 (2014) 1–14.
- [65] B. Lin, L.G. Zhao, J. Tong, H.J. Christ, Crystal plasticity modeling of cyclic deformation for a polycrystalline nickel-based superalloy at high temperature, Mater. Sci. Eng. A 527 (2010) 3581–3587.
- [66] J.C. Tucker, L.H. Chan, G.S. Rohrer, M.A. Groeber, A.D. Rollett, Tail departure of log-normal grain size distributions in synthetic three-dimensional microstructures, Metall. Mater. Trans. A 43 (2011) 2810–2822.
- [67] A. Acharya, A.J. Beaudoin, Grain-size effect in viscoplastic polycrystals at moderate strains, J. Mech. Phys. Solids 48 (2000) 2213–2230.
- [68] C.A. Sweeney, W. Vorster, S.B. Leen, E. Sakurada, P.E. McHugh, F.P.E. Dunne, The role of elastic anisotropy, length scale and crystallographic slip in fatigue crack nucleation, J. Mech. Phys. Solids 61 (2013) 1224–1240.